HUMS2025 Data Challenge Result Summary

Team Name: UNSW TMCM Group

Team Members: Nico Herwig, Pietro Borghesani, Wade Smith, Zhongxiao Peng, Robert Randall

Institutions: UNSW Sydney

Publishable: Yes, but code will not be provided

1. Summary of Findings

In the HUMS2025 data challenge, our team focused on identifying characteristic fault features of a gearbox casing crack. We started analysing vibration data from all sensors under 125% load, focussing first on the log amplitude spectrum. Two main fault symptoms were observed: (1) primary evidence of a planetary-ring related phenomenon was found in the growth of the 5th harmonic of planet-pass frequency, and (2) further supporting signs of ring damage were identified in a significant growth of high-frequency random vibration, whose envelope showed planetary-gear related modulating components.

Symptom (1) showed a clear progression from day 14 (around sample "Day014_20240507_102051_125%TT") onward, while symptom (2) was detectable from day 12 (Day012_20240501_110341_125%TT). Sensor 2, located nearest to the detected housing crack, exhibited the earliest and most pronounced fault indications, but clear evidence of symptom (1) was observed from all three casing mounted sensors (sensors 2, 3 and 4).

In addition to the frequency of the observed symptoms, the fact that they were only visible on casing mounted sensors confirms that they are unrelated to the artificial tooth crack on the pinion of the first stage. The fact that sensor 2, the closest to the housing crack, shows the strongest evidence of symptom (1) and the only evidence of symptom (2) further confirms the location of the crack.

Our interpretation is that the crack on the housing resulted in a deformation of the ring which in turn produced an unbalance in the meshing process of the planets as highlighted by the growth of the carrier-synchronous harmonic of symptom (1), which is not visible in the healthy condition (beginning of the test).

2. Description of Analysis Methods

All the sensors were treated with the same fundamental signal processing techniques and compared to the same theoretical gear meshing frequencies.

Raw log amplitude spectral analysis and comparison with the gear components

A high-resolution spectrum was generated using FFT applied to the full-length raw time-domain signals, and the logarithmic amplitudes were computed. The detected peaks were then compared to theoretical frequency components of the gear system, including multiples of the carrier and input shaft speed. This allowed the team to link each harmonic to a specific gear/shaft.

Order tracking and synchronous averaging

Order tracking and synchronous averaging were performed using a time-to-angle domain transformation based on the input shaft, as the tachometer was mounted on this shaft. Resampling was applied to ensure an integer number of samples per revolution, enabling precise synchronisation for averaging. Due to the complexity of the multi-stage gearing, this approach could not utilise the hunting tooth period and the resampling was instead iteratively applied across all shafts. The final order-tracked signals which were used to show fault symptoms are obtained with respect to the output shaft and contain 11,427 samples per revolution. Their synchronous averaging was performed over 171 output shaft revolutions. Order tracking sharpens peaks and minimises spectral leakage, allowing for a more reliable tracking of their amplitude throughout the experiment.

Identification of symptomatic high-frequency random vibration and their analysis

A significant and consistent growth of the spectral energy in the frequency range 14 kHz to 23 kHz was identified. This can be seen in Figure 1, where the log spectrum for sensor 2 of the first day and the last day are compared. To shed some light on its nature, envelope analysis was applied. The process began with bandpass filtering the signal in the range 18-20 kHz, where no apparent discrete peak was present. This frequency range was thus considered to contain only broadband random vibration components. After bandpass filtering, the signal was then transformed into its analytic form and the squared envelope was obtained.

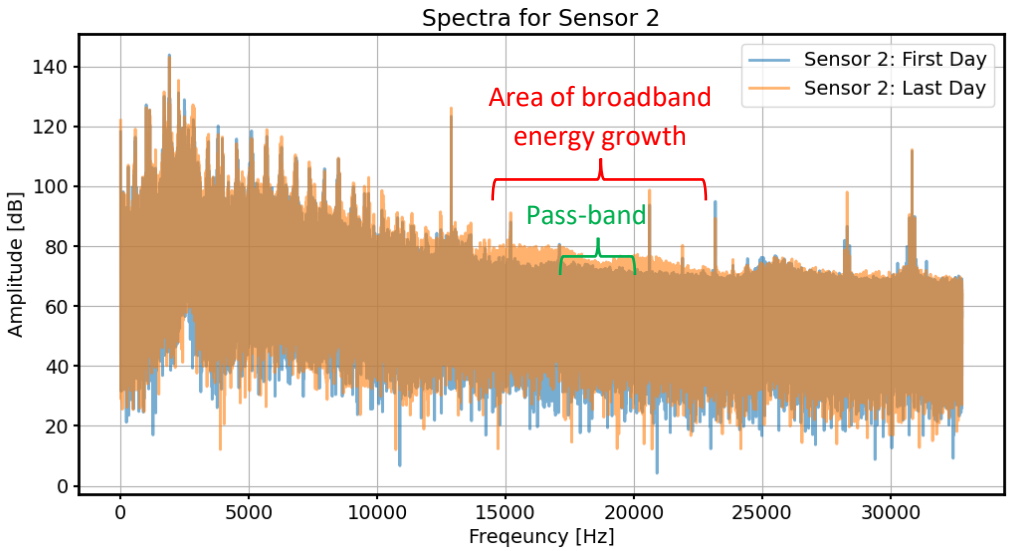

Figure 1: Log squared amplitude spectrum for sensor 2 for the first 125% load recording (blue) and the last 125% load recording (orange) for the entire frequency range.

Although the theoretical approach suggests conducting all steps prior to the final FFT in the time domain, followed by order tracking the signals demonstrated very stable shaft speeds. Thus, order tracking was applied first for simplicity. Theoretical frequencies were used as a reference for comparison throughout the analysis.

3. Key Fault Characteristics for Early Detection

In this section, we explore key fault characteristics that can be identified in the spectrum and envelope spectrum. Figure 2 illustrates the spectrum (left) and squared envelope spectrum (right) for Sensor 2 at distinct time points. For this analysis, data corresponding to 125% load was extracted from the dataset. As a reference, time 60 aligns with the sample labelled "Day011_20240424_140804_125%TT". The data is presented in terms of the output (carrier) shaft's orders. Sensor 2 was selected for this analysis because it is the most affected by the crack fault due to its proximity to the fault location.

Key symptomatic spectral harmonic

The symptomatic 20th harmonic of the carrier corresponds to approximately 114.6 Hz. At time 60, the 20th harmonic of the spectra in Figure 2 (left) is almost indiscernible from the background noise. However, at times 70 and 80, a clear and substantial peak is present. Additionally, it can be seen that other peaks remain substantially unaffected by the fault over time.

High-frequency broadband noise

The envelope analysis of the broadband noise in the range 18-20 kHz shows a growth of many planetary-stage related harmonics from time 60 to time 70. The predominant peaks in the envelope are located at a combination of sun and carrier harmonics, for instance the cluster of peaks between orders 30 and 45 in Figure 2 (right) correspond to $8 \times$ sun-shaft frequency $\pm$ $2N \times$ carrier frequency. This confirms that this growth of high-frequency vibration energy is related to the planetary stage. The fact that this growth is exclusive to Sensor 2 confirms the location of the crack (see also trending results of Figure 3).

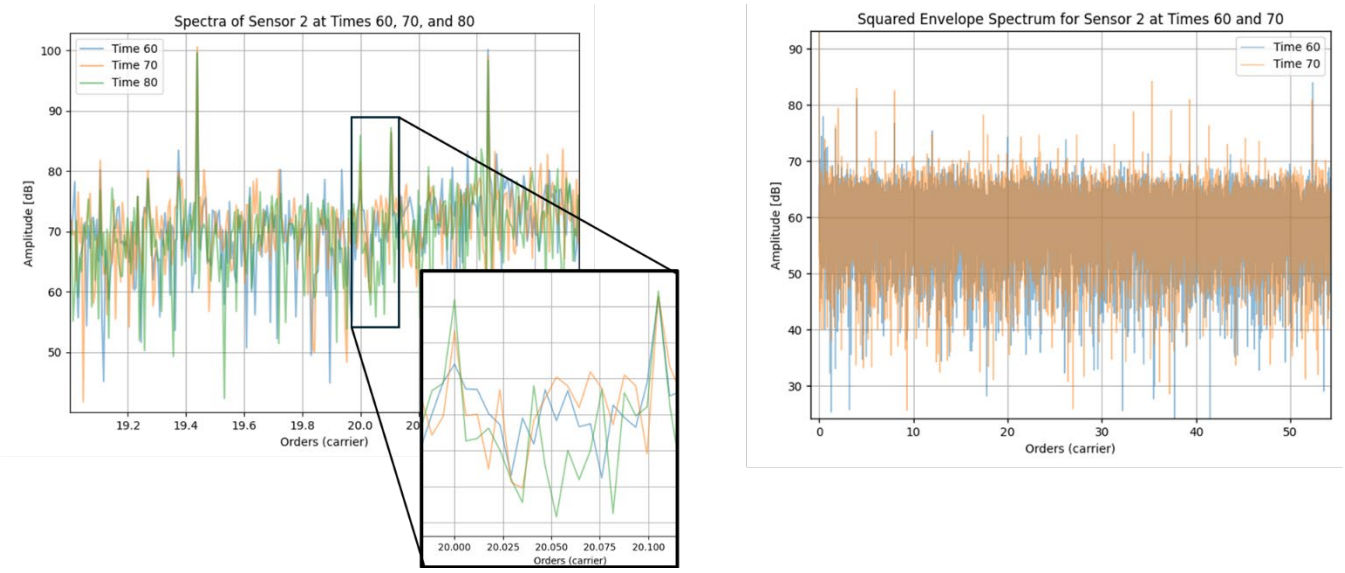

Figure 2: Spectra (left) and squared envelope spectra (right) for Sensor 2 at different times for 125% load.

4. Fault Progression Trending Curve

Figure 3 displays the RMS values of the 18-20 kHz band. Interestingly, the values of Sensors 2 and 3 are almost identical until around sample 62 [Day012_20240501_110341_125%TT], when the RMS of Sensor 2 rises sharply. From this point onwards, Sensor 2 begins to deviate significantly from Sensor 3 and the substantially stable trend of all other sensors. This increase in Sensor 2's RMS value indicates the onset of fault progression, highlighting its sensitivity due to its proximity to the fault source. The local nature of high-frequency vibration suggests that the fault is near Sensor 2, which is in fact the closest to the crack.

To further understand the fault's development, we also trended, for all sensors, the amplitude of the 20th harmonic of the output shaft in the spectrum of the synchronous average signal, for the 125% load case. This is shown in Figure 4, which reveals a notable increase in the amplitude from sample 70 onwards for Sensors 2, 3 and 4. Day014_20240507_102051_125%TT corresponds to sample number 70. This increase of the 5th harmonic of the planet-pass frequency can be linked to the housing crack which would likely result in a distortion of the ring.

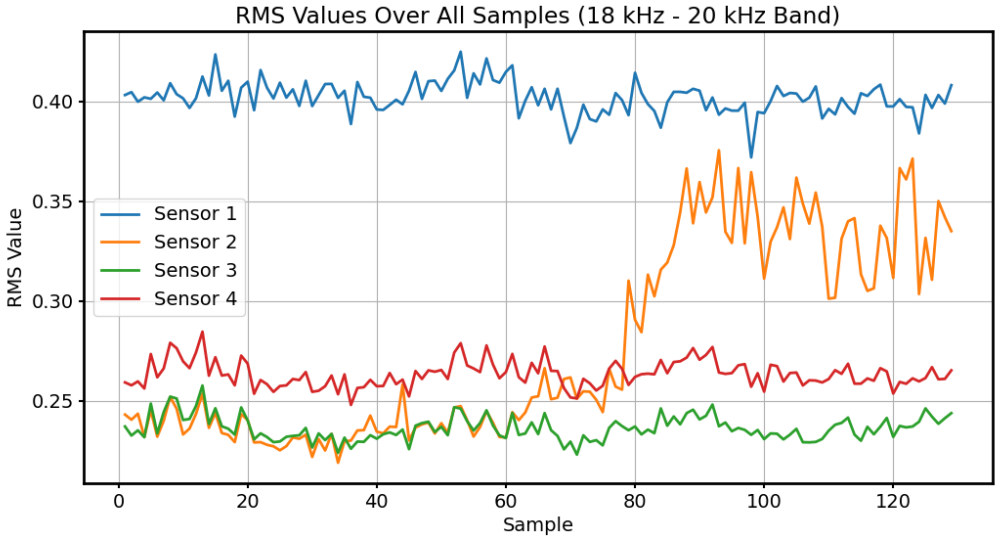

Figure 3: RMS value (125% load) of all sensors in the frequency band between 18 kHz to 20 kHz (linear scale, raw data units).

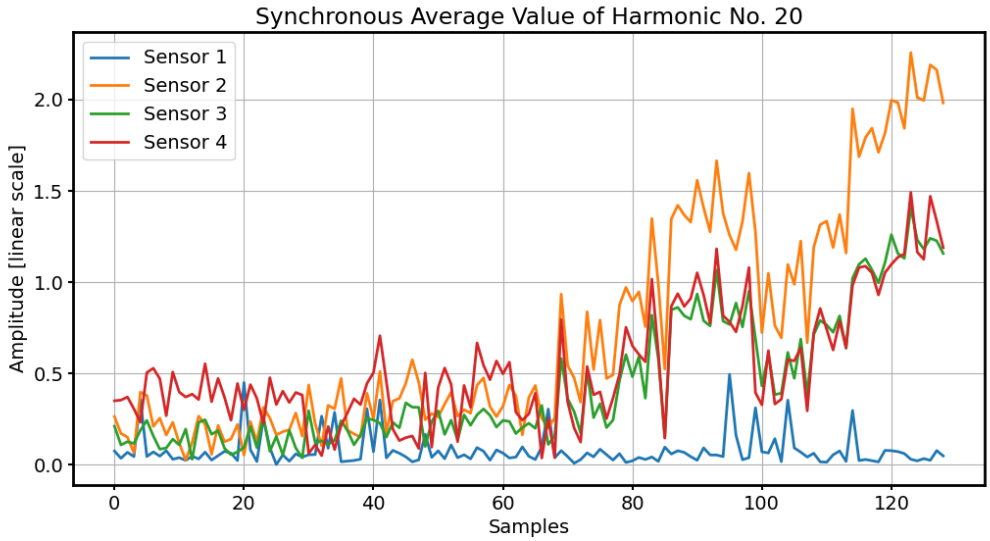

Figure 4: Spectral amplitude of the 20th harmonic of the carrier (~114.6 Hz) for all 4 sensors, 125% load.

To summarise the findings for the data challenge, the earliest convincing detection of the crack fault of the gearbox housing is found at sample 62 of the 125% load data, which is Day012_20240501_110341_125%TT. This can be seen analysing the high frequency content in Sensor 2. The modulation of this random vibration by planetary-stage related harmonics and the location of Sensor 2 suggest a localised fault near this sensor. Later, this diagnostic conclusion is further confirmed by analysing the spectrum of the synchronous averaged signals. The increase of the 20th harmonic of the output shaft for Sensors 2, 3 and 4 is very clear around Day014_20240507_102051_125%TT. This harmonic, which is a multiple of the planet-pass frequency, is almost indiscernible in the spectrum in the first stage of the tests. This suggests that a deformation of the ring, likely induced by the crack in the casing, has changed the overall vibratory behaviour of the planetary stage affecting all sensors installed on the gearbox itself.